A New Organization Metric for Synoptic Scale Tropical Convective Aggregation

Daeho Jin[1,2], Lazaros Oreopoulos[2], Dongmin Lee[3,2], Jackson Tan[1,2], Kyu-myong Kim[2]

[1] GESTAR-II, University of Maryland – Baltimore County, Baltimore, MD, USA
[2] Earth Sciences Division, NASA's Goddard Space Flight Center, Greenbelt, MD, USA
[3] GESTAR-II, Morgan State University, Baltimore MD, USA

Corresponding author: Daeho Jin (Daeho.Jin@NASA.gov)

Key Points:

- A new metric was developed to quantify the degree of organization of tropical convective systems at synoptic scales
- The new organization metric is optimized for multiple organized aggregates occupying sparsely large and noisy domains.
- The new metric successfully captures known synoptic convective behaviors, and is potentially applicable to a range of domain sizes.

Abstract

Organization metrics were originally developed to measure how densely convective clouds are arranged at mesoscales. In this work, we apply organization metrics to describe tropical synoptic scale convective activity. Such activity is identified by cloud-precipitation (hybrid) regimes defined at 1-degree and 1-hourly resolution. Existing metrics were found to perform inadequately for such convective regime aggregates because the large domain size and co-existence of sparse aggregate occurrences with noisy isolated convection often violate assumptions inherent in these metrics. In order to capture these characteristics, in this study the existing "convective organization potential" (COP) metric was modified so as to focus on local organization and provide increased weight to aggregate size. The resulting "area-based COP (ABCOP) follows the principle that the more numerous the objects, the higher the chance of organization. It is thus optimized to capture large-scale convective events occurring during phenomena such as ENSO and MJO, while also performs as well as existing metrics for small domain sizes.

Plain Language Summary

In meteorological applications, organization metrics examine the distribution of atmospheric objects and quantify how densely they are clustered together. Existing organization metrics characterizing convection were developed for small scales (e.g., mesoscale) convective activity, but were proven inadequate as measures of organization for coarsely resolved objects in large domains such as one-degree objects within a 40°×40° or larger domain. This is because large scale convective objects are sparse and form multiple local clusters, while existing metrics were designed to measure the organization level of the domain as a whole. In this study, we propose a new organization metric optimized for multiple local organizations, and tolerant to noisy isolated objects. A series of tests demonstrates the performance of the new organization metric in a host of cases with wide range of grid sizes.

1 Introduction

Atmospheric convection is one of the most important processes contributing to weather and climate variability. Individual tropical convective cores are usually of sub-kilometer to a few kilometer scales, while convective systems comprising several cores and anvil clouds often develop to scales of a few hundred kilometers (i.e., mesoscale convective system [MCS]), which is a major contributor to hydrological and radiation variability (Houze, 2004; Nesbitt et al., 2000 among many others). Moreover, aggregations of MCSs create large-scale features like mesoscale complexes (Laing & Fritsch, 1997) or "superclusters" (Chen et al., 1996; Mapes & Houze, 1993; Nakazawa, 1988).

Many models of various types appear to simulate organized convection spontaneously in large domains even with homogeneous boundary conditions and forcings, a behavior known as convective self-aggregation (see the review of Wing et al. 2017). Moreover, it has also been found that a higher level of organized convection results in the atmosphere being drier and less cloudy overall, and more efficient in cooling to space on average (e.g., Bony et al., 2020; Holloway et al., 2017; Windmiller & Craig, 2019; Wing, 2019; Wing et al., 2020). Considering the potential effect of self-aggregation on climate sensitivity through the control of humidity and cloudiness (e.g., Coppin & Bony, 2018; Cronin & Wing, 2017; Hohenegger & Stevens, 2016), the availability of proper measures of the degree of organization across a range of scales is important for climate studies.

The degree of organization of convective systems (i.e., how densely they are arranged in a limited region) can be quantified using a so-called *organization metric*. Tobin et al. (2012) suggested an organization metric called the “simple convective aggregation index” (SCAI), for aggregates identified by satellite-observed 0.5° brightness temperatures in 10°×10° domains (i.e., 20×20 grids). The basic idea of SCAI is that more organized scenes are composed of fewer convective systems that are closer to each other. Subsequently, White et al. (2018) and Xu et al. (2019) argued that the size of each convective system should be an important element in the definition of organization metrics, and introduced the “convective organization potential” (COP), and “modified SCAI” (MCAI) metrics, respectively. Independently, Tompkins & Semie (2017) developed an organization metric that compares the horizontal distribution of convective clouds to a purely random distribution (I_{org}), while Kadoya & Masunaga (2018) introduced the Morphological Index of Convective Aggregation (MICA) metric based on the area fraction occupied by convective clouds. Lastly, Retsch et al. (2020) developed the Radar Organization Metric (ROME) based on the same principle as COP but optimized for ground radar observations, while Brune et al. (2020) introduced the local wavelet-based organization index (LWOI) by modifying the previous WOI (Brune et al. 2018) to exploit the localization of wavelets both in space and time (details for some of these metrics are discussed in section 2).

Recently, Jin et al. (2020; J20 hereinafter) extended the convective aggregation analysis to the *synoptic scale* using the concept of “cloud regimes” (CRs; Oreopoulos et al., 2014, 2016). Based on regime identification at 1° resolution, J20 examined characteristics of convective aggregates (details about “aggregate” definition can be found in section 2.2), the sizes of which vary from a handful to hundreds of grid cells. However, gaps in coverage and the infrequent daily sampling were impediments to analyzing the aggregates in greater detail. Subsequently, Jin et al. (2021; J21 hereinafter) developed cloud-precipitation (hybrid) regimes (CPRs) also at 1° resolution by combining cloud and precipitation observations, and introduced a novel methodology to seamlessly extend convective regime identification to half-hour temporal resolution using these CPRs (details forthcoming in section 2.1). This new approach enabled examination of large-scale convective systems even at sub-daily time scales, something not feasible with J20’s cloud-only data.

Building on the work of J20 and J21, when we attempted to examine the temporal evolution of convective aggregates at synoptic scales we found that the application of existing organization metrics on our CPR-based convective aggregates produced results that were inconsistent with previous studies because the characteristics of large synoptic scale domains are notably different from those of smaller domains used for the development of existing metrics.

Simply put, in a large domain, multiple organized groups of aggregates can be distributed sparsely, a condition not captured well by existing metrics. This finding motivated us to develop a new organization metric optimized for synoptic scale phenomena, the topic of this paper. The methodology to identify CPR-based convective aggregates and the development of the new metric are described in sections 2 and 3. The characteristics of the new organization metric are discussed in section 4, and its performance relative to existing metrics for various domain sizes is provided in section 5. We conclude with a summary and discussion in section 6.

2 Identifying aggregates based on cloud-precipitation regimes

2.1 Cloud-precipitation (hybrid) regimes

Previously, J20 identified convective aggregates with tropical CRs derived from the Moderate Resolution Imaging Spectroradiometer (MODIS) Level-3 2-dimensional joint histograms resolving cloud fraction in predetermined bins of cloud optical thickness (COT) and cloud top pressure (CTP) at 1°×1° horizontal resolution (Platnick et al., 2018, 2003). A convective aggregate was defined as a group of adjacent grid cells assigned to CR1 (representing mixtures of convective cores and thick stratiform clouds), CR2 (cloud mixtures at various phases of the convective life cycle), and CR3 (anvil clouds), with CR1 presence being a prerequisite for the aggregate to be considered part of active convection.

In the subsequent work by J21, CRs were replaced by CPRs which combine cloud observations from MODIS with co-located precipitation information from the Integrated Multi-satellitE Retrievals for GPM (IMERG; Huffman, Bolvin, et al., 2019; Huffman, Stocker, et al., 2019; Tan et al., 2019; IMERG V06 Final Run). J21 found that in the case of a CPR set derived from equally-weighted cloud and precipitation information in the clustering procedure, it was possible for certain CPRs of substantial precipitation intensity and areal coverage to be predicted by solely precipitation information, with high accuracy exceeding 90%. This means in practice that the full diurnal cycle of select CPRs can be reconstructed at the half-hour resolution of IMERG without swath gaps.

Among J21's 19 CPRs derived with equal cloud-precipitation weighting in the 15°S-15°N tropical domain, CPR1 and CPR2 had the heaviest precipitation with high cloud top (low CTP), large COT, and near overcast coverage (cloud fraction > 94%), and were deemed to represent the grid cells containing convective cores and adjacent thick stratiform clouds (Figs. 1a and 1b). When comparing coincidences of CPR1 and CPR2 to J20's tropical CRs, we were able to confirm that grid cells assigned to CPR1 and CPR2 co-occur mostly with tropical CR1 (not shown). These two most convective CPRs are therefore used for identifying convective grid cells in this study.

For this study, the reconstruction of these two CPRs was based on one-hour resolution IMERG data from June 2000 to May 2021. Specifically, one-hour IMERG data was obtained by averaging the original half-hour IMERG data after smoothing with a 1-2-1 filter, which reduces the noisy fluctuations of half-hour data shown in J21 (e.g., their Fig. 10). The IMERG transition from TRMM to GPM as the reference for calibration in June 2014, does not seem to have introduced a discontinuity in the timeseries of the combined relative frequency of occurrence (RFO) of one-hour reconstructed CPR1 and CPR2 in the tropics (Fig. 1f).

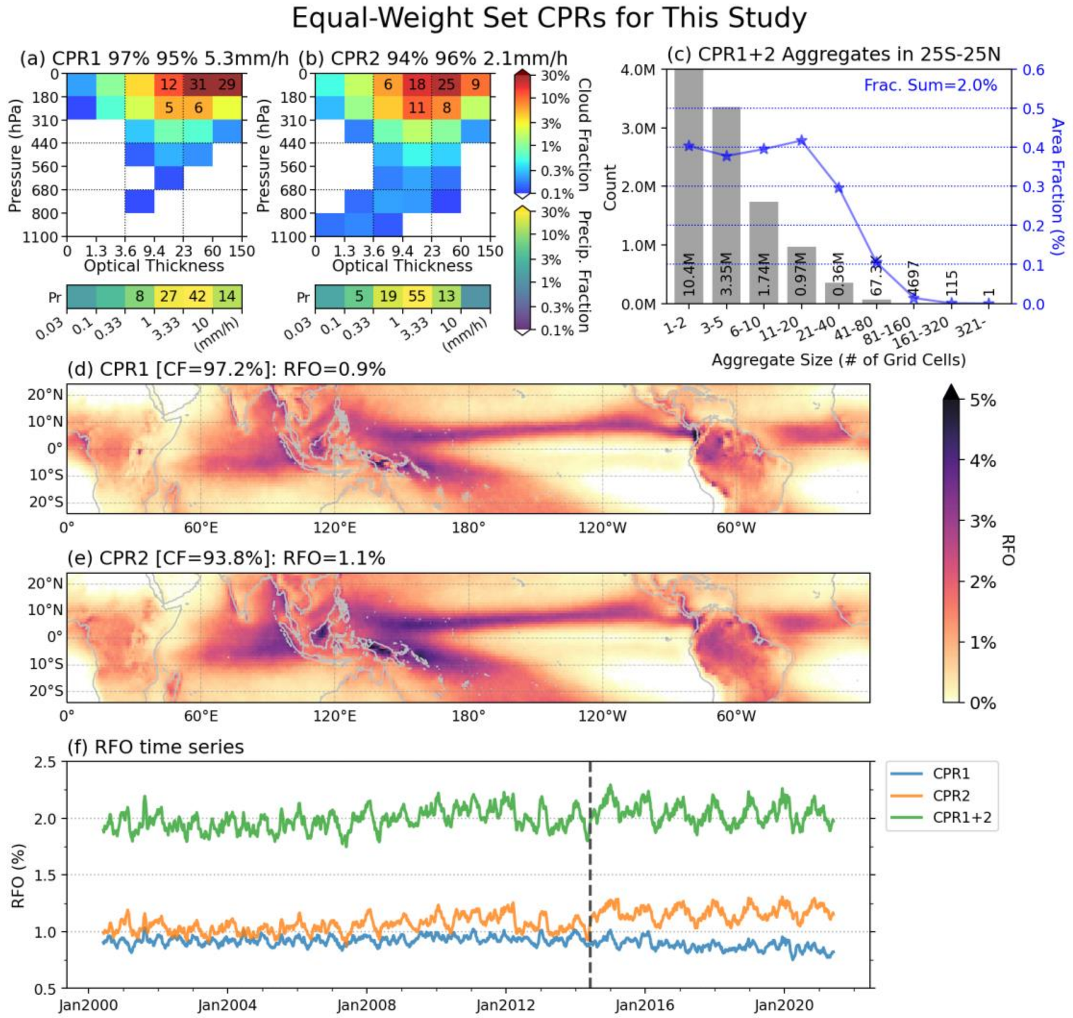

Figure 1. Cloud-precipitation “hybrid” regimes (CPRs) derived in the deep tropical domain (15°S-15°N) from cloud and precipitation histograms that are equally weighted (referred to as Cld42+Pr6x7 set in Jin et al. 2021) in the clustering procedure. (a), (b) Centroids of the cloud and precipitation components of hybrid regimes CPR1 and CPR2, (c) The number count (gray histogram) and areal fraction (blue line and star symbol) of CPR1+2 aggregates as a function of size in the extended domain 25°S-25°N, and (d), (e) geographical distribution (relative frequency of occurrence [RFO]) of the reconstructed CPR1 and CPR2. (f) smoothed pentad (5-day mean; 7-pentad running mean) timeseries of CPR1 RFO (blue), CPR2 RFO (orange), and their combined RFO (green) for the extended tropical domain of 25°S to 25°N. The vertical dashed line demarcates the IMERG transition of calibration reference from TRMM to GPM (June 2014).

The RFO maps of reconstructed CPR1 and CPR2 (Figs. 1d and 1e) are largely consistent with the RFO maps of the original CPR1 and CPR2 in Fig. 5 of J21, as well as with the RFO pattern of J20's CR1, including RFO peaks at the Intertropical Convergence Zone (ITCZ), South Pacific Convergence Zone (SPCZ), and Indo-Pacific warm pool regions. On the other hand, the reconstructed CPRs have greater chance of occurrence over the islands of Borneo and New Guinea than the original CPRs. This deviation is because convection and associated rainfall activity are weaker during the overpass times of the Terra and Aqua satellites in accordance with the known diurnal variability in this region (e.g., Worku et al., 2019).

2.2 Identification of aggregates

The definition of "aggregate" in this study is essentially the same as in J20, i.e. adjacent grid cells assigned to either CPR1 or CPR2 ("CPR1+2" aggregate hereinafter). The only deviations from the J20 definition are that the absence of one of the two regimes does not disrupt the aggregate (since both CPR1 and CPR2 largely correspond to previous CR1), and that a diagonal connection is allowed. As shown in the snapshot of CPR aggregates in Fig. 2b, synoptic scale convective superclusters sometimes form quasi-linear patterns where the diagonal connection plays a key role in identifying an aggregate. The statistical distribution of resulting aggregates shows the expected exponential decrease of aggregate counts with size (expressed as the number of 1° grid cells), which can exceed even 200 grid cells in extreme cases (Fig. 1c).

The occurrence pattern of CPR1+2 aggregates is consistent to that of IMERG precipitation of heavy intensity because the CPRs in this study are predicted by precipitation information, as illustrated in the snapshot example of Fig 2. To provide additional context we also added in this figure the distribution of outgoing longwave radiation (OLR) and brightness temperature (Tb) for the near-simultaneous scene (Figs. 2c and 2d) from Atmospheric Infrared Sounder (AIRS; Kahn et al., 2014; Susskind et al., 2014) observations, and from the NCEP/CPC Merged IR dataset (Janowiak et al., 2017). These datasets show quite a consistent pattern with the CPR (and precipitation) distribution. However, it can be seen that the areas occupied by CPR1+2 grid cells are slightly smaller than the dark-colored area (low OLR/Tb, representing high and thick cloud). For example, no heavy precipitation is registered by IMERG near the southern tip of India, an indication of the somewhat subjective nature of identifying the most active convection.

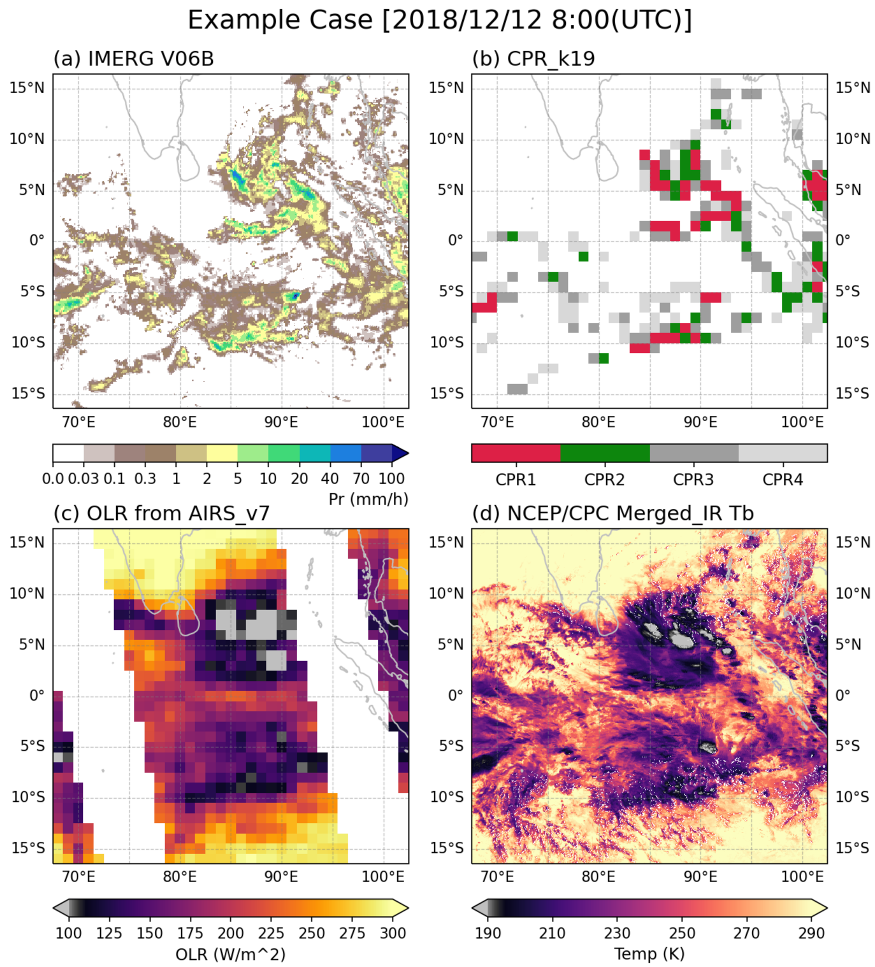

Figure 2. A snapshot of (a) precipitation rate from IMERG, (b) occurrence of selected CPRs, (c) outgoing longwave radiation (OLR) from AIRS, and (d) brightness temperature (Tb) from NCEP/CPC merged IR data on 2018/12/12. The select coordinated universal time (UTC), 8:00 is the closest time to the Aqua satellite passing time on the equator in the eastern tropical Indian Ocean (around 85°E).

3 Development of a new organization metric

3.1 Review of existing organization metrics

The basic idea in the convective organization potential (COP) metric developed by White et al. (2018) is to measure the proximity of aggregates using the concept of “interaction potential” (*V*). For two aggregates, *i* and *j*, *V* and COP are defined as:

$$V(i,j) = \frac{r_i+r_j}{d(i,j)}, where\ r = \sqrt{Area/\pi} \qquad (1)$$

$$COP = \frac{\sum_{i=1}^{N-1}\sum_{j=i+1}^{N} V(i,j)}{\frac{1}{2}N(N-1)} \; for \; N \geq 2 \tag{2}$$

where r_i and r_j are the nominal radii (radii of equal area circles) of aggregates *i* and *j*, *d(i,j)* is the distance between their centers, and *N* is the total number of aggregates in the domain. COP is then the average of *V* for *all available pairs* of aggregates. More organized systems are represented by higher values of *V* (larger aggregates closer to each other), and thus COP. The upper limit of value *V* is 1 in the ideal case of two perfectly circular tangential aggregates. However, the shapes of realistic convective aggregates are far from circles (e.g., Fig. 5 in later subsection), so *V* values can exceed 1. The Radar Organization Metric (ROME) is a variant of COP optimized for ground radar observations (Retsch et al., 2020). In ROME, the interaction potential is changed to the distance-weighted sum of aggregate area, but the process of averaging the interaction potentials for all pairs is the same as in COP. A value of ROME can be defined even in the case of sole aggregate, which is not so for COP.

The simple organization index (I_{org}) developed by Tompkins & Semie (2017) measures the relative organization level of aggregates compared to the idealized random distribution, using the cumulative distribution function (CDF) of nearest-neighbor distance (NNCDF). The authors considered the idealized distribution as a Poisson point process, the CDF of which is given by the Weibull distribution (Chiu et al., 2013; Weger et al., 1992):

$$NNCDF_{random}(d) = 1 - \exp\left(-\lambda \pi d^2\right) \tag{3}$$

where λ is the normalized count, i.e. the number of aggregates per unit area, and *d* is the nearest-neighbor distance. I_{org} is then defined for a given number of aggregates in a domain as the integrated area of actual NNCDF along the axis of $NNCDF_{random}$ for a range of nearest-neighbor distances ($0<r<$maximum distance in a domain; see Fig. 18 in Tompkins and Semie, 2017). An I_{org} value of 0.5 represents then an organization level similar to that of a randomly distributed scene, while higher values (up to 1) indicate more organized scenes.

Actually, the organization metric with the longest history is the simple convective aggregation index (SCAI) proposed by Tobin et al. (2012) and defined as the product of normalized distance between aggregates and normalized number of aggregates:

$$SCAI = \frac{N}{N_{max}} \frac{D_0}{L} \times 1000 \tag{4}$$

where N and N_{max} are the number of aggregates and the maximum number of aggregates in the domain, respectively, *L* is the domain's characteristic length, and D_0 is the geometric mean of distances between all available pairs of aggregates (called "order-zero diameter"). Later, Xu et al. (2019) proposed the modified SCAI (MCAI) whereby D_0 was replaced by D_1 ("order-one diameter", the arithmetic mean of distances), and the aggregate size was taken into account in the distance term (i.e., "inter-object distance"; defined as D_2 by combining them).

The basic idea behind the SCAI and MCAI is that the mean distance of aggregate pairs is expected to be inversely proportional to the number of aggregates in a domain, hence a smaller number of aggregates clumped together is a well-organized ideal scene. However, the assumptions behind SCAI and MCAI seem inappropriate for synoptic scale convective systems in large domains. For our dataset and domains, we found the D_0 and D_2 values to be nearly constant regardless of aggregate population (Supplementary Fig. S1). As a result, SCAI and MCAI values depend heavily on the number of aggregates so that scenes with larger numbers are interpreted as less organized, which is counterintuitive (see also Figs. 8 and 9 in White et al., 2018). The assumptions of SCAI fail in the present study because the density of convective aggregates is quite low (mostly under 0.08 with peaks at around 0.15 in 40×40 grid domain; see Supplementary Fig. S2).

Lastly, Kadoya and Masunaga (2018) proposed the Morphological Index of Convective Aggregation (MICA), defined as the product of two area ratios, namely convective cloud area over the smallest rectangle enclosing all convective clouds, and outside-the-rectangle area over the total domain. This metric works well for small rectangular domains where a group of organized aggregates occurs in one side of the domain while the other side is clear. However, it is not suitable for the case of multiple sparsely distributed groups of organized aggregates, which is a common occurrence in our dataset.

Taking all this into consideration, we selected the COP and I_{org} metrics as the main benchmarks in this study against which to compare our new organization metric. (SCAI and MCAI results are shown in Supplementary materials.) The characteristics of these metrics are summarized in Table 1.

Table 1. Summary of existing organization metrics considered in this study

	Description	Factors to consider	Weakness in synoptic scale study
COP	Domain mean interaction potential for all available pairs	▪ Size of object (*r*) ▪ Distance between two object centers (*d*)	No consideration for local organizations
I_org	Comparison of cumulative distribution function (CDF) of distance to nearest neighbor (NNCDF) to that in randomly distributed scene	▪ Number of objects (*N*) ▪ Nearest neighbor distance (between centers)	No consideration for objects' size
SCAI	Normalized mean distance for all available pairs	▪ Number of objects (*N*) ▪ Distance between two object centers (*d*)	Dominated by number of objects in low density

	multiplied by normalized number of objects		conditions (more objects, less organized)
MCAI	Similar to SCAI, but modified measure of distance to consider the objects' size	▪ Number of objects (*N*) ▪ Distance between two object boundaries (d-r_i-r_j)	Same as SCAI

3.2 New organization metric

Previously, White et al. (2018) showed values of SCAI and COP for a few simplified examples on a 20×20 grid (reproduced below in Fig. 8 and Supplementary Fig. S11). Similar idealized experiments but on a 40×40 grid with more complex situations (motivated by our sample area analyzed in this study) are shown in Fig. 3 to examine the characteristics of COP and I_{org}. Figures 3a, 3b, and 3c assume three groups of organized aggregates, with an isolated cloud subsequently added (Fig. 3c). The only difference between Figs. 3a and 3b is the aggregate size in the upper left corner. As noted earlier, since I_{org} does not consider aggregate sizes but only the location of their centers, the value of I_{org} remains unchanged between Figs. 3a and 3b, while the value of COP increases from 0.163 to 0.199 (+22.1%) indicating stronger organization in Fig. 3b than 3a.

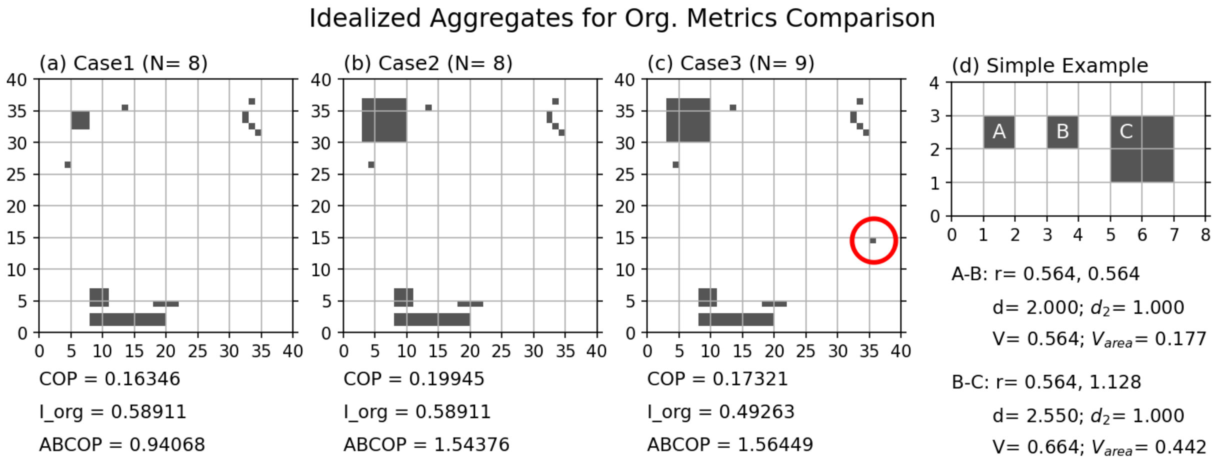

Figure 3. Comparison of organization metrics for synthetic scenes comprising three groups of organized aggregates (panels (a) and (b)), and with an isolated convective element subsequently added (panel (c); red circle). *N* is the total number of aggregates. Panel (d) is a simple example demonstrating the relationship between aggregate size and interaction potential (*V*).

The only difference between Figs. 3b and 3c is the addition of a single grid cell of an isolated convective element on the right side (in red circle). This small difference would be intuitively perceived as a negligible change in convective organization, but both COP and I_{org} nevertheless decrease notably, from 0.199 to 0.173 (-13.1%) and 0.589 to 0.493 (-16.3%).

For this problem, our conclusion is that COP is optimized for assessing the organization level for the whole domain, but its skill in assessing local organizations in a sparsely populated environment is lacking. For example, COP is defined as the "average" of interaction potentials (V) for "all available pairs" (Eq. 2). However, for the circumstances shown in Fig. 3, the interaction with surrounding neighbors seems more appropriate (like I_{org} which considers the nearest neighbor only). Moreover, a notable decrease in the value of COP with the addition of an isolated object is unavoidable when the metric is normalized by the number of objects (i.e., "averaging"). Hence, the first set of modifications we propose is: (1) for each aggregate, selecting the pair providing *maximum* interaction potential, and (2) *summing* these select interaction potentials.

Secondly, after testing various approaches on a wide range of sample scenes, we found that the current form of interaction potential does not give sufficient weight to the size of the aggregate. As shown in Fig. 3d, for the comparison of A-B pair with B-C pair, the size of C, which is quadruple the area of A, is represented only as twice as large in terms of nominal radius. In addition, the distance between non-tangential aggregates in rectangular coordinates increases for larger aggregates. As a result, the interaction potential of the B-C pair (0.664) is only 17.7% greater than that of the A-B pair (0.564). In order to rectify this problem, we propose a second set of modifications: (3) modifying the interaction potential to use the area rather than the radius of aggregates, and (4) changing the distance from "center-to-center" to "(outer) boundary-to-boundary", as in MCAI (referred to as "inter-object distance" in Xu et al. 2019).

Based on these four changes, a new modified COP, which we call the "*area-based convective organization potential*" (ABCOP) is defined as:

$$d_2(i,j) = max\left[1, d(i,j) - r_i - r_j\right] \tag{5}$$

$$V_{area}(i,j) = \frac{\left(\frac{A_i+A_j}{2}\right)/A_{domain}}{d_2(i,j)/L_{domain}} \tag{6}$$

$$ABCOP = \sum_{i=1}^{N} max\left[V_{area}(i,j)\right]_{j\neq i} \ for\ N \geq 2 \tag{7}$$

where $d(i,j)$ is the distance between the centers of aggregates i and j, and r_i and r_j are their nominal radii; $d_2(i,j)$ is hence meant to represent the nominal distance between the boundaries of the two aggregates. A_i and A_j are the areas of the aggregates, and L_{domain} is a length scale calculated as the square root of domain area, A_{domain}; N is the total number of aggregates. Finally, the unitless V_{area} represents then mean areal density of the two aggregates over their normalized distance. ABCOP in the case of sole aggregate (N=1) is discussed in the subsection 4.1.

As noted earlier, because the shapes of real aggregates are far from circular, d_2 can be close to zero or even assume negative values in extreme cases, which can be problematic since it appears in the denominator of Eq. 6. Hence, the minimum value of d_2 is set to 1 to prevent odd results. When testing several values from 0.2 to 1 as candidates for the minimum value of d_2, we found that the behaviors of the new interaction potentials were very similar, but smaller minimum values had a tendency to produce much larger value of V_{area}, and thus ABCOP. (We assume units of grid cells [or pixels]. If other units are employed, minimum value of 1 should be changed to that representing one grid cell size.)

With this new area-based interaction potential, values in the previous simple example shown in Fig. 3d change from 0.564 to 0.177 for A-B pair, and from 0.664 to 0.442 for B-C pair, which corresponds to a 150% increase for the pair of quadruple-sized aggregate (cf. +17.7% with original V). In addition, for the cases of Figs. 3a-3c, since ABCOP is more sensitive to the size of aggregates by definition, it results in a 64.1% increase from Figs. 3a to 3b (0.941 to 1.544). The added isolated cell in Fig. 3c results in only a 1.3% increase of ABCOP, which is notably different from (and better than) COP (-13.1%) and I_{org} (-16.4%).

4 Characteristics of the new organization metric

4.1 Properties of the new organization metric

The upper limit of V_{area} can be obtained by assuming that the mean area of A_i and A_j cannot be larger than the half of domain area with non-overlap condition, and $d_2 \geq 1$:

$$V_{area}(i,j) = \frac{\left(\frac{A_i + A_j}{2}\right)}{A_{domain}} \times \frac{\sqrt{A_{domain}}}{d_2(i,j)} < \frac{\sqrt{A_{domain}}}{2} \tag{8}$$

Hence, V_{area} can be quite a large number depending on the domain size, and an upper limit of ABCOP is hard to predict due to summation operation (e.g., extreme cases would be composed of large aggregates surrounded by many small aggregates). In the domains selected for this study (typically 40×40 grid) with CPR1+2 aggregates, most values of ABCOP are below 2 (see Fig. 6 in the next subsection).

Even though ABCOP is a unitless metric, caution should be exercised when comparing its values between domains of different sizes. For example, assuming exactly the same distribution of two aggregates (i.e., the same mean area of aggregates and same distance between them) in domains X and Y, V_{area} values depend on the size of domains X and Y according to Eq. 6, specifically they will differ by the factor $1/L_{domain}$, and a bigger domain will yield smaller V_{area} (thus ABCOP, too), i.e. less organized. This gets magnified when the areal sizes of the two domains being compared are substantially different. Still, if the relative size of the aggregates with respect to the domain matters, the smaller ABCOP values in the bigger domain have the physical interpretation that the areal density of the same aggregates is lower in the bigger domain than the smaller domain.

The case of a sole aggregate in the domain is problematic for most organization metrics (except ROME). The behavior of ABCOP for this single aggregate case is examined in the Appendix. The essence is that the value of ABCOP varies according to how the situation is interpreted. For example, if it is assumed that this situation resulted when one of two aggregates moved far away from the other and left the domain, the lowest value of interaction potential in Appendix Eq. A5 would be the best choice. If on the other hand it is assumed that the aggregate resulted from two aggregates moving towards each other and ultimately merging, the highest value would be the right answer. In this study, we consisder the first assumption as making ABCOP more consistent with other organization metrics which assume zero value for this very rare case. Hence, ABCOP in this special case is defined as:

$$ABCOP = V_{area}(i) = \frac{\sqrt{\pi}}{2}\frac{Density\_A_i}{2-\sqrt{Density\_A_i}}\ for\ N = 1 \tag{9}$$

where the *Density_A*$_i$ is defined as A_i/A_{domain}. Eq. 9 (derived in the Appendix) is set with the (semi-) lowest limit value of ABCOP by applying a *loosely approximated* maximum length in the domain. As a result, while ABCOP increases when two aggregates get closer and closer, as soon as they are connected, ABCOP becomes substantially smaller. For example in the case of Fig. 3d where only A and B aggregates exist (i.e., no C aggregate) in the domain of a 8×4 grid, ABCOP's value changes from $1/\sqrt{32} \approx 0.177$ to $\frac{\sqrt{\pi}}{2}\frac{0.0625}{1.75} \approx 0.032$ when A and B are connected. However, as mentioned above, the definition of ABCOP for the single aggregate case can be adapted to the situation. For example, if ABCOP is applied to the small-scale scenes where large single aggregate should be more emphasized, the alternate definition of ABCOP producing the highest value in Eq. A5 would be a better choice.

Lastly, it is also worth to noting that, like other metrics, by applying the concept of "nominal" radius, ABCOP does not consider the specific shape of individual aggregate. Hence a squall line and hurricane have the same effect on ABCOP if their areas (i.e., number of grid cells) are the same. Furthermore, ABCOP only considers the size of the domain, but not its shape.

4.2 Performance of the new organization metric for synthetic scenes

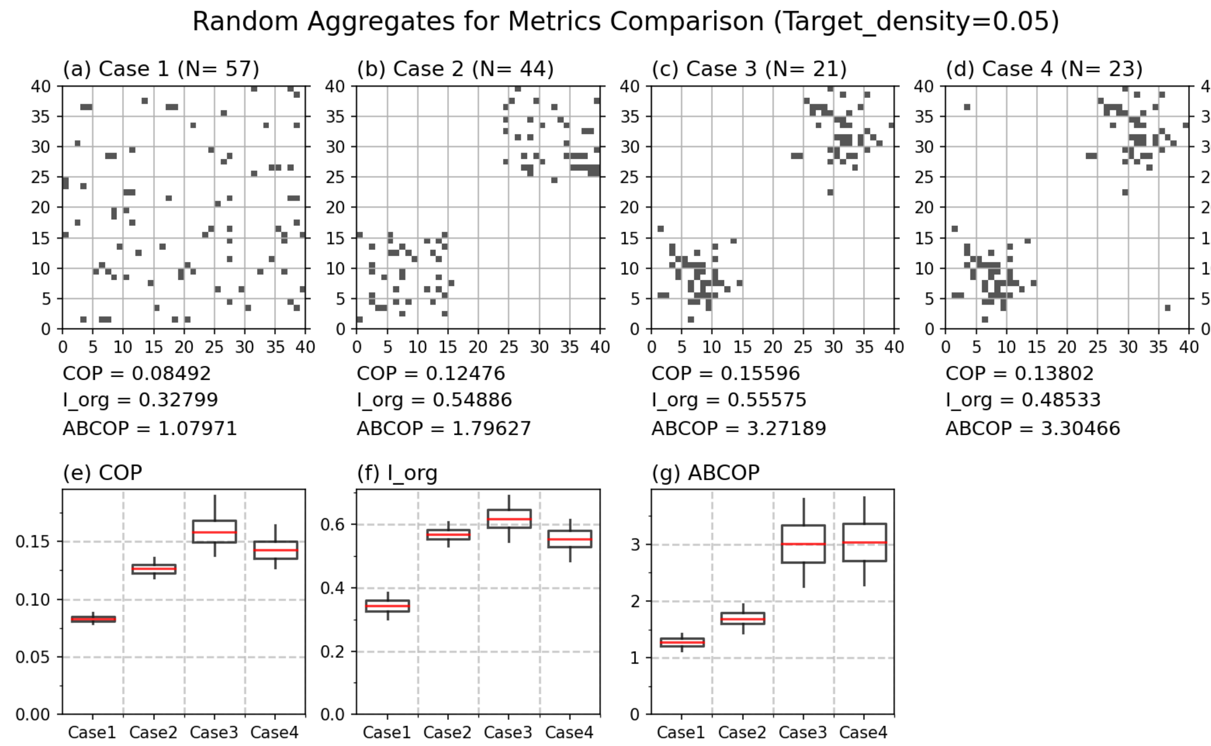

Figure 4. Comparison of organization metrics for synthetic scenes with: (a) uniform random distribution (Case 1); (b) uniform random distribution in limited area (32% of total area; Case 2); (c) Gaussian random distribution with two centers (Case 3); and (d) same as (c) but with two additional objects in opposite corners (Case 4), while the areal density remains unperturbed (5%). *N* is the total number of aggregates. Panels (e)-(g) show box-whisker plots of the distribution of organization metrics for 1000 random realizations of synthetic scenes representing cases 1-4. Whiskers indicate 5% to 95% range, boxes inter-quartile range, and red lines median values.

For a more rigorous test than the ideal cases of Fig. 3, we performed experiments with four different cases, each consisting of 1000 randomly generated samples of fixed areal density of aggregates (or objects) (Fig. 4). Cases 1 and 2 assume uniform random distribution in the whole area (case 1) and limited region (case 2; meant to be more organized than case 1). In case 3, a random Gaussian distribution was applied in the similar parts of the domain as case 2 in order to increase its organization, producing larger aggregates near the center of the Gaussian distribution. Case 4 is exactly same as case 3 except for the addition of two isolated objects in the previously unoccupied corners. We expect that cases 3 and 4 would be identified as the most organized scenes to a similar degree.

The variability of each organization metric for these 1000 samples is displayed in the form of box-whisker plot in the bottom row of Fig. 4. The performances of COP and I_{org} are generally consistent to the results shown in Fig. 3. Both perform well for identifying differences in the relative organization levels among cases 1-3. They differ slightly however in that I_{org} tends to identify case 2 as relatively more organized (thus close to case 3) than COP. This is likely caused by the fact that I_{org} counts for only location, but not aggregate size. For the last case, the addition of the two isolated grid cell objects to the scene of case 3, results in the notable deviation (suppression) of COP and I_{org} values, as in the examples of Figs. 3b and 3c.

On the other hand, ABCOP also properly captures the evolution of the level of organization for cases 1-3, but with a relatively smaller increase from case 1 to case 2. In addition, the range of values for case 4 is nearly identical to that of case 3, as it should (Fig. 4g). One important difference of ABCOP is that the range of values is much wider than those of COP or I_{org} for cases 3 and 4. This is because of the sensitivity of ABCOP to the aggregate size. Indeed, the higher values of ABCOP for cases 3 and 4 stem from scenes in which a large aggregate is surrounded by several satellite aggregates, which ABCOP preferentially sees as very organized compared to scenes of a few medium-sized aggregates surrounded by fewer satellite aggregates.

4.3 Real-world performance of the new organization metric

We now evaluate the new organization metric ABCOP against existing metrics with real scenes of tropical CPR1+2 aggregates We select four target domains for this analysis based on the occurrence map of CPRs 1 and 2 (Figs. 1d and 1e): (1) the tropical Indian Ocean (TIO; 50°E-90°E, 20°S-20°N; 40×40 grid), (2) the Maritime Continent (MC; 95°E-145°E, 15°S-15°N; 30×50 grid), (3) the western tropical Pacific (WTP; 150°E-170°W, 20°S-20°N; 40×40 grid) and (4) the Amazon basin and its vicinity (AMZ; 80°W-40°W, 25°S-15°N; 40×40 grid). The size of domain, 40°×40° is large enough to cover the theoretical ascent areas of various equatorial waves (Yang et al. 2003). Figure 5 shows scenes sampled from the WTP domain, with figures for other domains provided in Supplementary Figs. S4, S5, and S6.

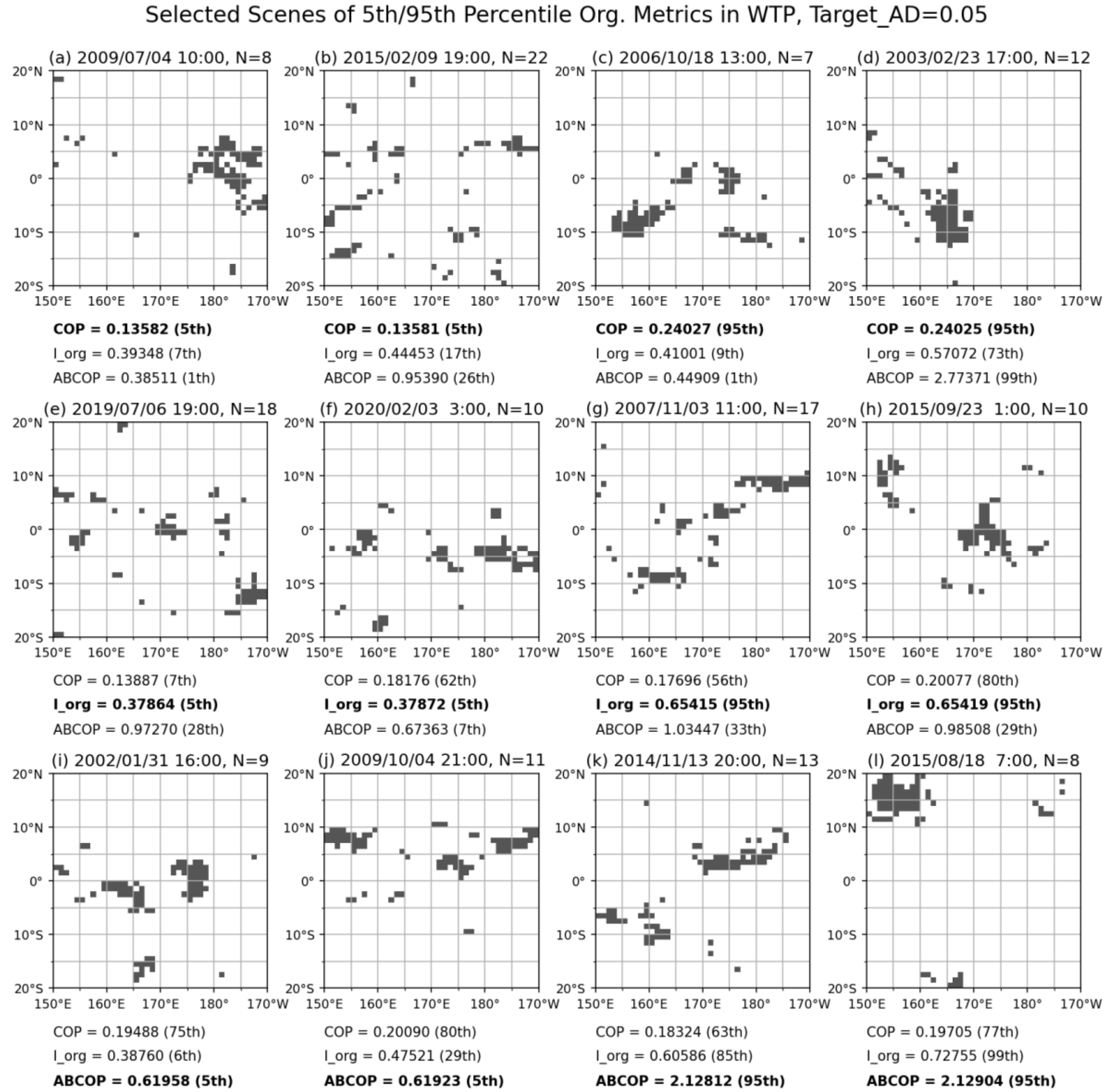

Figure 5. Select scenes of fixed 5% (±0.25%) areal density with organization metric values in 5th (left two columns; less organized), and 95th percentiles (right two columns; more organized) for (a)-(d) COP, (e)-(h) I_{org}, (i)-(l) ABCOP for in the western tropical Pacific domain (WTP; 150°E-170°W, 20°S-20°N). Above each panel we provide the observation time and number of aggregates (N), and each organization metric's percentile value is after its numerical value.

Figure 5 shows real scenes corresponding to 5th (left two columns; less organized) and 95th percentile (right two columns; more organized) of each organization metric, COP (top row), I_{org} (middle row), and ABCOP (bottom row). In the top row, COP clearly distinguishes between the less organized scene of Fig. 5b and the two organized scenes of Figs 5c and 5d. In the case of Fig. 5a, a big aggregate on the right side of the domain makes the scene to visually appear as organized, but the value of COP (and ABCOP, too) is quite low. This is an example of the weakness of measuring interaction potential: no satellite aggregates near a big aggregate means no (or weak) interaction potential. On the other hand, the scene of Fig. 5c is quite interesting in that large aggregates look organized according to COP, but not close enough in the view of ABCOP whose value for Fig. 5c is lower than that for Fig. 5b. This shows the salient COP feature of making an average of interaction potentials, which gives greater chance of perceived organization for the scenes consisting of fewer aggregates. COP samples in other domains (shown in the Supplementary Figures) also show that more organized scenes always have fewer aggregates, typically less than 15, compared to the less-organized scenes.

I_{org} results shown in the middle row seem to be most affected by isolated objects. Because I_{org} only considers the location of objects and not their sizes, pairs of small objects close together in Figs. 5g and 5h make it identify these scenes as more organized. On the other hand, sparsely existing isolated objects in Figs. 5e and 5f make the scenes identified as less organized. For the same scenes, ABCOP reports consistently low values because of the small sizes of close pairs in Figs. 5g and 5h.

In the case of ABCOP, comparison of Figs. 5i and 5l where the scenes contain similarly small number of total aggregates (N), the values of ABCOP are dramatically different, with greater organization suggested for Fig. 5l. The key difference between the two scenes is the proximity of satellite aggregates surrounding a big aggregate. This example shows that, similarly to the case in Fig. 4c, ABCOP tends to identify a scene as more organized when a big aggregate is surrounded by several aggregates, due to the summation being performed. In contrast, COP suggests that both scenes are similarly organized, with values around 75th percentile; the relatively lower COP value for the scene of Fig. 5l is mainly because it averages for “all available” pairs.

4.4 Dependence of the new organization metric on areal density

One of the modifications of ABCOP from its COP ancestor was the change from averaging to simply summing the interaction potentials (see also Table 2). This translates to higher chances of larger value of ABCOP (more organized) with a higher population (or density) of objects, something examined in Fig. 6 where the distributions of the three organization metrics are shown as a function of areal density.

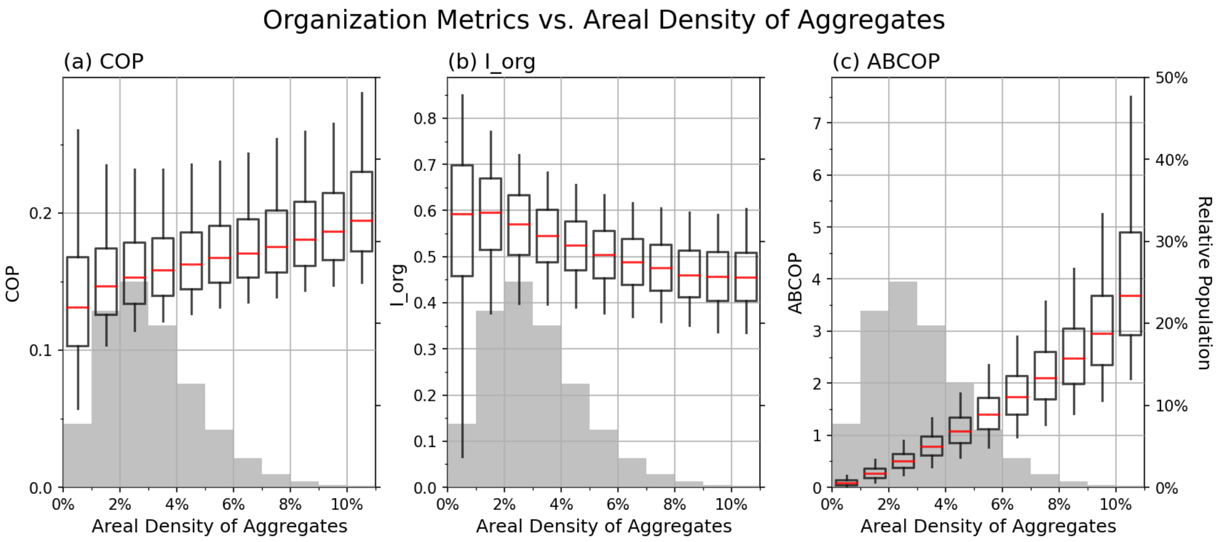

Figure 6. Distribution of (a) COP, (b) I_{org}, and (c) ABCOP values as a function of the areal density of aggregates for all four domains (TIO, MC, WTP, and AMZ). The vertical width of the box indicates the interquartile range (25th to 75th percentile), and whiskers extend from 5% to 95% percentiles. The red line shows median values. The gray bars provide a visualization of the relative distribution of scene population by areal density.

While ABCOP values increase with areal density, as expected, the rate of increase seems faster than linear. In addition, the variability of values also increases with areal density. These patterns indicate that ABCOP behaves in a way consistent with the proposition that *there are higher chances of organization with more individual convective cells*. While COP also shows increase of values by areal density, the rate of increase is relatively weak, and the interquartile ranges overlap greatly for nearby areal density bins. It is also notable that some of the extremely large values of COP come from the population of lowest areal density bin (less than 1%). In the case of I_{org}, values generally decrease for higher areal density, and this probably reflects the fact that the reference random distribution ($NNCDF_{random}$ in Eq. 3) approaches unity faster with a greater number of objects (assuming that the number of aggregates is generally proportional to the areal density).

The fact that COP and ABCOP increase with areal density is actually important for large-scale climate studies. This is because responses to notable climate variability like the Madden-Julian Oscillation (MJO) or El Niño–Southern Oscillation (ENSO) are usually associated with dramatic changes in the convective system population. For example, the MJO, defined as a convective envelope propagating eastward near the equator from the Indian to the Pacific Ocean with a 40 to 50-day period (Madden & Julian, 1971, 1994), has active and inactive phases in specific regions, and both the size and population of convective aggregates increase significantly in the active phase compared to the inactive phase (Supplementary Fig. S8). As a result, an organization metric that is generally proportional to the areal density enables it to capture the climate variability effectively.

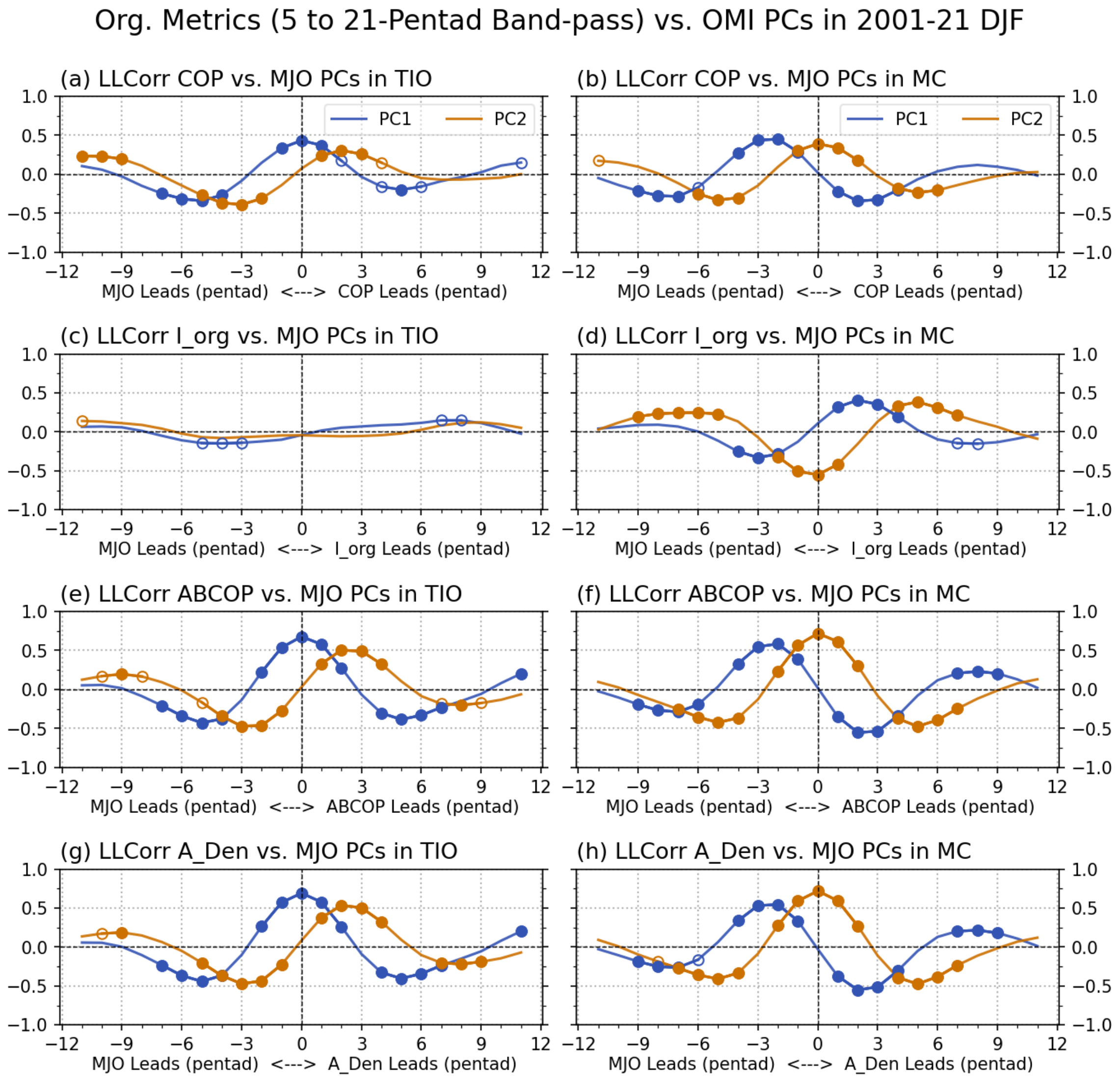

Figure 7. Lead-lag correlation coefficients between OMI PCs, transformed to pentad (5-day mean), and band-pass filtered anomalies (5 to 21 pentads) of organization metrics in the boreal winter seasons (December to February). The left column shows results in the tropical Indian Ocean (TIO; 50°E-90°E, 20°S-20°N) and the right column in the Maritime Continent (MC; 95°E-145°E, 15°S-15°N). (a), (b) COP, (c), (d) I_{org}, (e), (f) ABCOP, (g), (h) Areal Density (A_Den). Open and closed circle symbols indicate that the correlation coefficients are above the two-tailed 90% and 95% significance levels, respectively, estimated using degrees of freedom accounting for autocorrelation.

To demonstrate this, Fig. 7 shows lead-lag correlations between organization metrics and MJO indices. We chose the OLR-based MJO index (OMI; Kiladis et al. 2014), which is known as more sensitive to convective systems than other dynamics-based MJO indices, to represent the MJO. OMI consists of the first and second principal components (PC1 and PC2) of the filtered OLR field, which correspond to the most active convection in the tropical Indian Ocean (TIO) and Maritime Continent (MC), respectively. We calculated organization metrics in the TIO (50°E-90°E, 20°S-20°N) and MC (95°E-145°E, 15°S-15°N) domains over the 21 boreal winter seasons (December to February in 2001-2021). The lead-lag correlation analysis shows that ABCOP as well as areal density itself captures the effect of MJO as expected. In the TIO domain, OMI PC1 is simultaneously (zero-lag) correlated with ABCOP and areal density (Figs. 7e and 7g). The PC2 peak follows after two to three pentads (10-15 days) of PC1 peak, and then is followed by the negative PC1 peak after another two pentads. This result is consistent with the approximate 50-day repeat period of MJO convective characteristics. Similar to ABCOP and areal density, the response of COP to the MJO also captures the in-phase relationship, but with relatively weaker correlations. In the case of I_{org}, the smaller correlation coefficients are even out-of-phase in the MC domain (Fig. 7d).

Comparing the MJO responses in the TIO and MC domains, I_{org} in particular shows different correlation magnitudes for the two domains, probably due to the different nature of convective systems, namely large sized systems in open oceans vs. small but numerous systems over land or complex layouts like the Maritime Continent (e.g., Yuan & Houze, 2010). Supplementary Fig. S8 also confirm that when the active MJO phase composite is compared to the inactive composite, the increase of mean size is more notable in the TIO domain while the count increase is more substantial in the MC domain. These characteristics may affect the behavior of I_{org}. For example, in the TIO domain, correlations of I_{org} are very weak likely because I_{org} does not consider object size. ABCOP, on the other hand, seems to respond well to changes of both size and count. The performance of ABCOP is also outstanding in response to ENSO (Supplementary Fig. S10).

In summary, based on the above examples, our new proposed ABCOP metric represents best multiple organizations in large and noisy domains, and thus performs well for convective activity at synoptic scales. In the following section, we examine how the performance of the new metric varies when domains of drastically different sizes are considered.

5 Performance of the new organization metric in other domain sizes

5.1 Scale, resolution, and domain size

As noted in the previous sections, existing organization metrics were optimized for more highly resolved convection in smaller domains (i.e., mesoscale), while the newly developed ABCOP was shown to work well for large scale features (i.e., synoptic scales). However, the numerical definition of either the previously defined organization metrics or ABCOP does not actually consider the scale directly. The most important factor included in any organization metric is the distribution of objects, commonly represented numerically by the distance between two objects. (Some organization metrics like COP and MCAI also consider the size of aggregates.)

Our calculation of organization metrics has been performed with data implicitly (synthetic cases) or explicitly (real cases) mapped onto an equidistant cylindrical grid that employs Cartesian coordinate system where the distance between two objects was measured in units of grid size. Under this convention, the true physical scale cannot be inferred from grid size (= number of grid cells) since resolution is not fixed. For example, Tobin et al. (2012) examined the organized convection using 10°×10° segmented domains with 0.5-degree data, thus the scenes consisted of cells arranged in a 20×20 grid. After Tobin et al. (2012), the performance of succeeding organization metrics like MCAI and COP were intercompared with SCAI in such 20×20 grid as well as in (their own) much larger grid (i.e., higher resolution in similar or larger domains; White et al. 2018; Xu et al. 2019). A large grid increases the chances of multiple organized objects occurring throughout the domain, thus resulting in probably different performances of organization metrics compared to those in small 20×20 grid scenes. However, this factor was not considered in the previous studies.

Our ABCOP metric was originally motivated by synoptic scale convective aggregates, but with the numerical definition, strictly speaking, optimized for scenes of large grids where multiple organized objects occur and are sparsely interspersed with noise; test scenes in this study are mostly of low density, usually less than 0.1 in a 40×40 grid (Supplementary Fig. S2). We therefore need to test the performance of ABCOP for two widely different domain sizes, a 20×20 small grid, and an oversize 360×50 grid representing the whole tropics. This is done in the next two subsections.

5.2 Small domain case

Previous works on organization metrics used select reference examples to intercompare performances. One example composed of four scenes (our Fig. 8) was introduced originally in Fig. 2 of Tobin et al. (2012), and reproduced later in Fig. 4 of White et al. (2018) for the purpose of comparing COP and SCAI. We note first that diagonal connections are prohibited when identifying aggregates in this small domain environment, and second that for unknown reasons the value of COP is slightly different from that in White et al. (2018) only for Fig. 8a; those of the other scenes are the same.

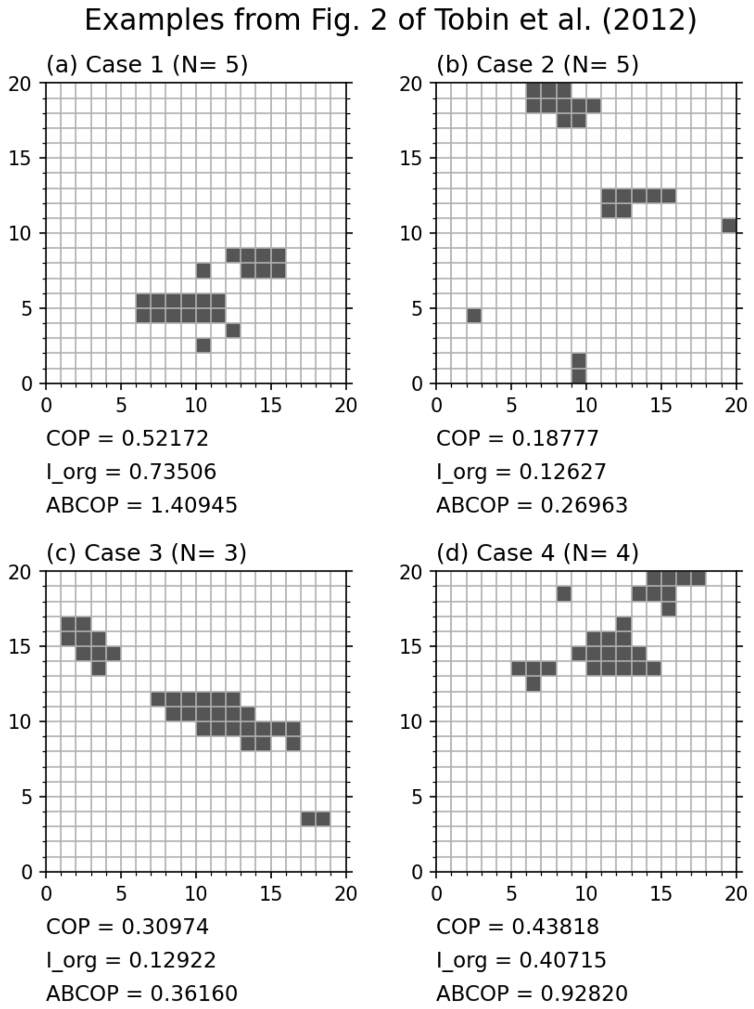

Figure 8. COP, I_{org}, and ABCOP computed for the four example scenes in Fig. 2 of Tobin et al. (2012), also shown in Fig. 4 of White et al. (2018).

For the examples with five or fewer aggregates on a 20×20 grid, COP works well as indicated by case 1 being identified as the most organized and case 2 the least organized scene. I_{org} also shows similar results except the value for case 3 that is relatively low, close to the value for case 2. For these examples, ABCOP shows the same order of organization levels as COP and I_{org}. In addition, White et al. (2018) showed another idealized example in their Fig. 5, and this is reproduced in Supplementary Fig. S11. The performance of ABCOP is generally consistent to that of COP with the scenes containing bigger aggregates identified as more organized. ABCOP deviates from COP in that its value increases more rapidly as aggregate sizes increase owing to the greater weight given to object size in the ABCOP definition.

Moreover, in an attempt to draw more generalized conclusions, we performed the evaluation of metrics with many randomly generated scenes, similar to the earlier Fig. 4. The top row in Fig. 9 shows a single sample from the 1000 stochastically generated realizations of each case. Case 1 represents small aggregates distributed randomly, thus is the least organized scene, while case 2 represents the most organized scene with big aggregates near the center. Case 3 contains two organized aggregations, but looks less organized than case 2 when assessed over the whole domain. Similarly to Fig. 4d, case 4 is identical to case 3 except for two isolated objects at opposite corners.

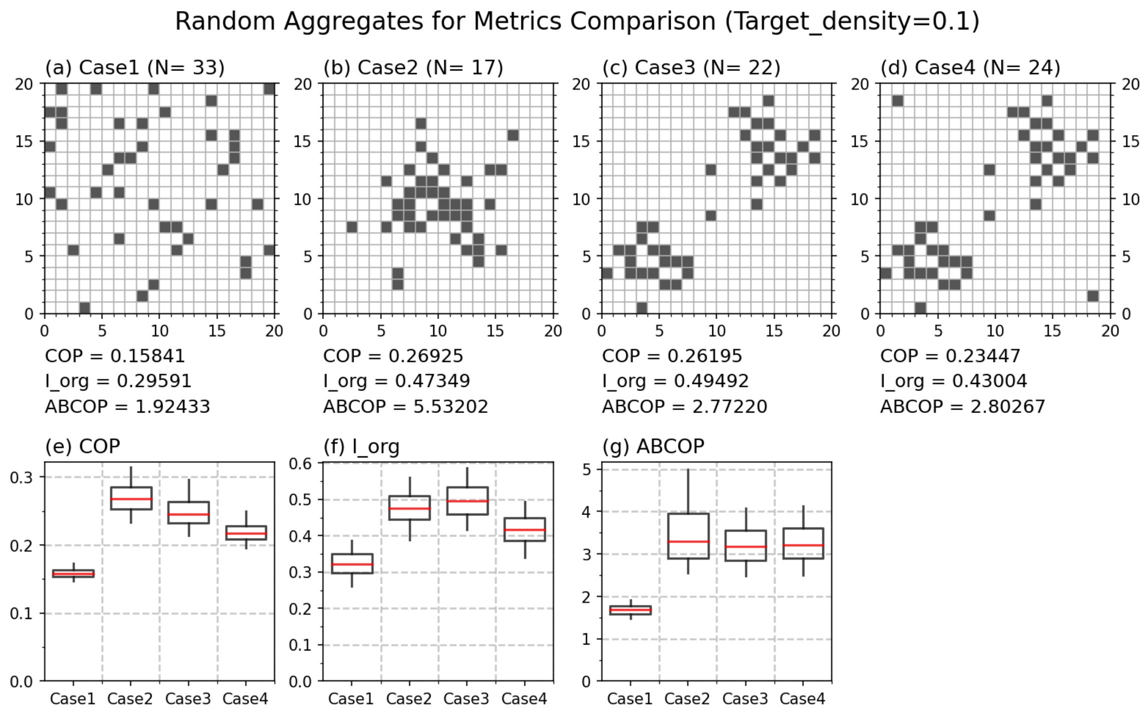

Figure 9. Similar to Fig. 4, but for smaller 20×20 grid with target areal density 0.1. Case 1 represents uniform random scenes, case 2 a single Gaussian random distribution in the center of the domain, and case 3 consists of two Gaussian random distributions. Case 4 is identical to case 3 except for two additional isolated objects at opposite corners.

For these cases, we note interesting difference between COP and I_{org}. COP, which considers all available pairs of aggregates, identifies case 2 as the most organized scene, while I_{org}, which considers the distance to the nearest neighbor, identifies case 3 as the most organized scene. Similar to the example case of Fig. 8, ABCOP's values imply that it assesses the degree organization as being somewhere between COP and I_{org}; for example, case 3 is identified as slightly less organized than case 2, but the differences are not as notable as that of COP. For case 4, ABCOP is the only one to show similar level of organization with the addition of two isolated objects to case 3, echoing the corresponding example in Fig. 4. However, one can argue that in this case where the domain is smaller, the addition of isolated objects should decrease the degree of organization of the scene. In this sense, the behavior of ABCOP that identifies case 4 as (slightly) more organized can be perceived as unphysical. We also note that the performances of SCAI and MCAI resemble that of COP for these cases (not shown). In summary, the various organization metrics have their own diverse characteristics for such a small 20×20 grid domain. ABCOP seems to work at least as effectively as existing organization metrics under these conditions.

5.3 The tropics as a single large domain

In this subsection, motivated by the work of Bony et al. (2020), we compare the performance of organization metrics in the whole extended tropical domain (25°S-25°N). Bony et al. (2020) employed I_{org} in the 30°S-30°N domain to investigate the relationship between tropical radiation budget and convective organization. With our CPR data at one-degree and one-hour resolution, the combined RFO of CPR1 and CPR2 is consistently near 2% as shown in Fig. 1f, and so is the areal density of CPR1+2 aggregates (Fig. 10), which is quite a low density with a narrow range compared to our previous 40×40 domains.

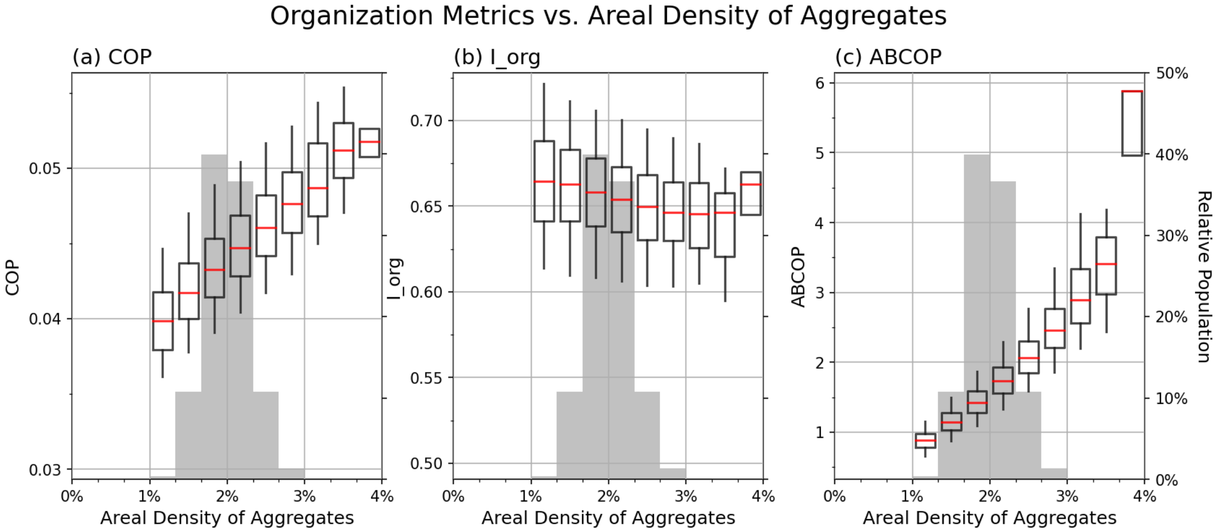

Figure 10. Same as Fig. 6, but for whole tropics (25°S to 25°N).

First, we examine the distribution of organization metrics as a function of areal density. The fundamental behaviors of the three organization metrics are similar to those shown in Fig. 6, namely positive slope of COP and ABCOP and negative slope of I_{org}. The COP slope looks steeper here, but actual value is slightly smaller than that in Fig. 6. In the case of I_{org}, values are generally higher than those in Fig. 6; median values are now around 0.65 here compared to below 0.6 in Fig. 6. The whole tropical domain is composed of a huge number of grid cells (360×50=18000), but deep convective systems occur mostly in the limited region of the upwelling branch of atmospheric circulation (Figs. 1d and 1e). This environment shares some similarity to case 3 of the small domain (Fig. 9c) where the higher sensitivity of I_{org} to the nearest neighbor distance contributed to its relatively high value. We also examined select real scenes by 5th and 95th percentiles of each organization metric as in Fig. 5, but visual inspection is not as helpful in this instance due to the low density of aggregates in a huge domain (Supplementary Fig. S12).

Previously, Bony et al. (2020) showed the simultaneous negative relationship between I_{org} anomaly and net radiation anomaly at top-of-atmosphere (TOA; referred to as Net_TOA (downward positive); their Fig. 6a), but found no significant relationship between I_{org} and ENSO. This issue is examined in Fig. 11 where lead-lag correlations are shown for de-seasonalized and smoothed (3-month running mean) monthly anomaly timeseries of organization metrics, Niño3.4 index, and Net_TOA from the CERES SYN1deg dataset (Doelling et al. 2016).

In terms of general trend, the timeseries of the organization metrics COP, ABCOP, and areal density (A_Den; black lines in Figs. 11a, 11e, and 11g, respectively) share some similarity; for example, less organized and populated on average in the 2002-2009 period and more organized and populated during the 2009-2012 and 2014-2016 periods. In the case of I_{org}, the timeseries has a “V” shape trend with a minimum (least organization) around 2011. However, lead-lag correlation patterns are similar between COP and I_{org}. Both metrics have simultaneous negative correlations with Net_TOA which is consistent to the results of Bony et al. (2020), and follow the variability of ENSO index a few months later. ABCOP and A_Den have no notable simultaneous relationships with either ENSO index or Net_TOA anomaly. Recall that in the case of organization metrics in the Maritime Continent domain, active (inactive) convection activity occurred near-simultaneously with La Niña (El Niño), but COP and I_{org} exhibit a reverse relationship by reporting less (more) organization in La Niña (El Niño) period (Supplementary Fig. S10).

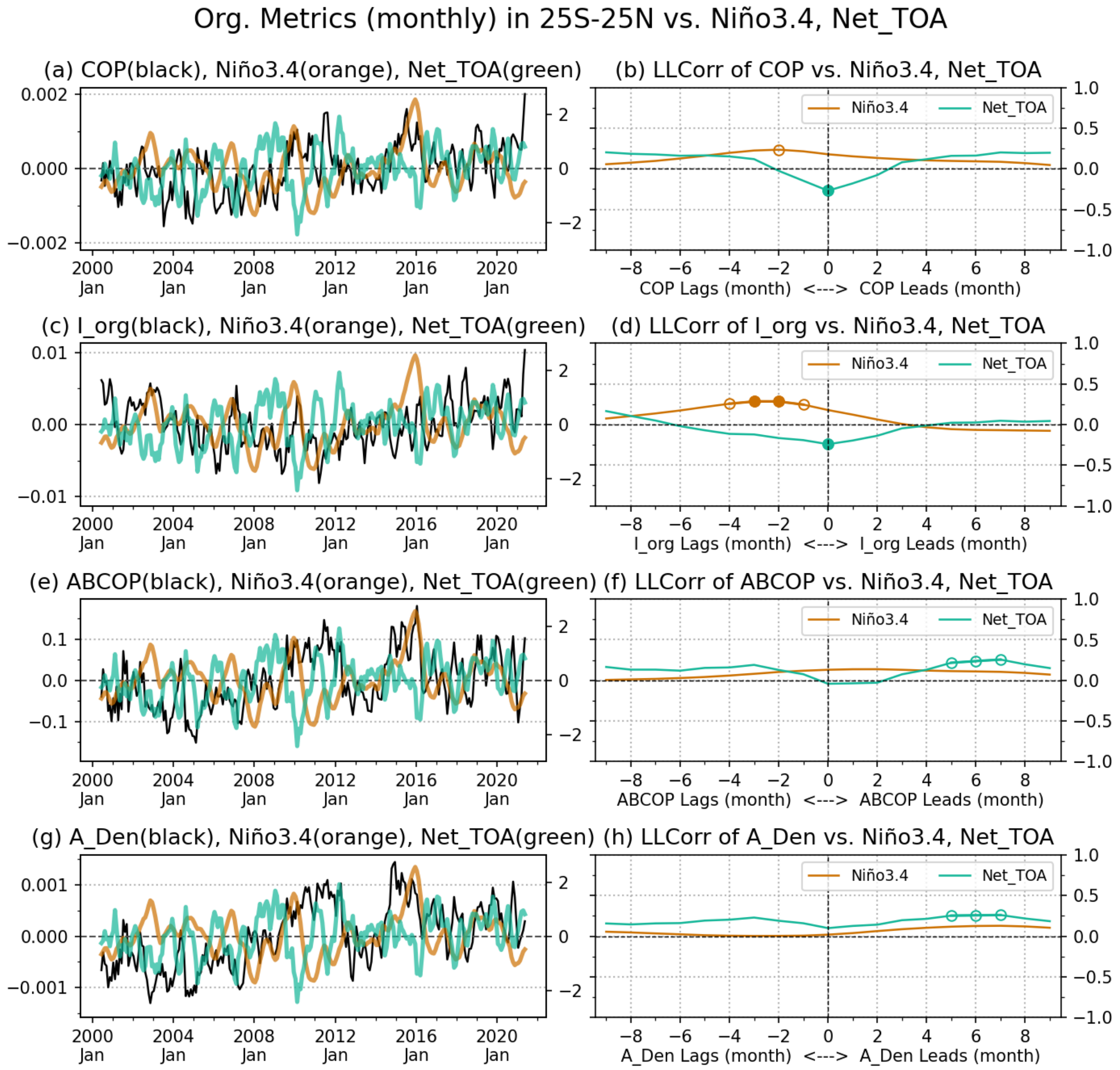

Figure 11. Lead-Lag correlation coefficients between monthly anomaly of organization metrics and Niño3.4 index and CERES net radiation anomaly at TOA (Net_TOA). The left column shows timeseries of organization metrics (black), Niño3.4 index (orange, in K), and Net_TOA (green, in Wm^{-2}), which are de-seasonalized and smoothed by a 3-month running mean. The right column shows lead-lag correlation coefficients where open and closed circle symbols indicate confidence levels above the 90% and 95% significance, respectively. (a), (b) COP, (c), (d) I_{org}, (e), (f) ABCOP, and (g), (h) Areal density (A_Den) of CPR1+2 aggregates.

The negative relationship between I_{org} and Net_TOA led Bony et al. (2020) to argue that most organized scenes are composed of smaller area where convective systems are clumped together while the areas of (relatively) clear sky were extensive and resulting in increased loss of radiative energy to space. The proposition itself makes sense physically, but we think that it merits a more sophisticated analysis that examines whether a third factor, namely areal density, can affect the negative relationship. For example, I_{org} values tend to decrease (indicating less organization) as areal density increases (Figs. 6b and 10b), which can contribute to the negative relationship, i.e., both the decreasing I_{org} value and increasing Net_TOA can be traced back to enhanced occurrence of convective systems. Moreover, the significance of negative relationship between I_{org} and Net_TOA (and ENSO index) is not consistent across the 21-year period. We tested the same calculations for sub-periods, 2000 to 2013 and 2008 to 2021 (each 13-year), and found that the negative correlation coefficient was stronger in the earlier years while hardly significant in the later years (Supplementary Figs. S13 and S14). Correlations with Niño3.4 are also different depending on the selected period. While inconsistencies in the IMERG timeseries may be contributing to this changing relationship, the relationship between I_{org} and Net_TOA based on our CPR-based analysis is still dubious. Considering the complex features of the radiative effects of various cloud types, this issue should be further investigated with more detailed analyses.

6 Summary and Conclusions

Organization metrics are a convenient way to describe how densely convective events are distributed in a limited domain. Such metrics were originally designed to examine small scale convection in satellite, model, and radar observations. In this study, we extended the application of organization metrics to the synoptic scale with larger grids. A seamless and temporally highly resolved cloud-precipitation (hybrid) regime dataset developed by J21 served as the basis for identifying convective aggregates consisting of 1° grid cells and for calculating organization metrics in large domains (40×40 or 30×50 grids).

Our regime dataset indicates that existing metrics are inadequate for large domains where sparse occurrences of multiple organized aggregates often violate assumptions inherent in the metrics. In order to rectify this problem, we introduced the following modifications in the pre-existing convective organization potential (COP):

(1) The definition of distance was changed from “between centers” to “between outer boundaries.”

(2) The radius-based interaction potential of COP was changed to an area-based form normalized by domain size.

(3) Interaction potentials were calculated for only one pair per aggregate providing maximum interaction potential, and they were then summed up instead of averaged over all pairs.

Table 2. Modifications of COP to obtain ABCOP.

COP		**ABCOP**

$d(i,j)$ *(Distance between two centers)*	(1) ➔	$d_2(i,j) = max\left[1,\ d(i,j) - r_i - r_j\right]$ *(Distance between two boundaries)*
$V(i,j) = \frac{r_i + r_j}{d(i,j)}$ *(Interaction potential)*	(2) ➔	$V_{area}(i,j) = \frac{\left(\frac{A_i + A_j}{2}\right)/A_{domain}}{d_2(i,j)/L_{domain}}$ *(Area-based interaction potential)*
$COP = \frac{\sum_{i=1}^{N-1}\sum_{j=i+1}^{N} V(i,j)}{\frac{1}{2}N(N-1)}\ for\ N \geq 2$ *(Averaged over all pairs)*	(3) ➔	$ABCOP = \sum_{i=1}^{N} max[V_{area}(i,j)]_{j\neq i}\ for\ N \geq 2$ *(Summed over pairs of maximum V_{area})*

The comparison of the performance of the new ABCOP against existing organization metrics for domains of various sizes and cases that include synthetic and real scenes, the latter consisting of CPR1+2 aggregates, shed light on the pros and cons of each metric. COP works well for identifying the organization level of the domain as a whole (e.g., case 2 of the small domain in Fig. 9), but tends to overestimate (underestimate) the organization level for scenes with fewer (more) aggregates (e.g., Fig. 5c). I_{org} has a good sensitivity on local organization (e.g., case 3 of Fig. 9), but tends to underestimate the organization of scenes containing big aggregates because it ignores size. On the other hand, ABCOP shows similar performance to COP and I_{org} in various simple cases, but with the additional advantage of being *tolerant to the noise of isolated aggregates*, something that existing metrics do not handle well. Moreover, existing metrics imply weak or even opposite responses of convective organization to notable climatic features like MJO and ENSO, which generate dramatic changes in both the population and size of convective systems at their various phases. ABCOP captures the known relationships of these climate features in a way consistent with our empirical and expert knowledge of how convection behaves.

While ABCOP is a unit-less metric, caution should be exercised when comparing ABCOP values for significantly different domain sizes as discussed in subsection 4.1. In addition, the scenes that ABCOP identifies as greatly organized tend to be those containing a few big aggregates surrounded by many satellite aggregates. For this kind of scenes, the ABCOP value can increase drastically, which is the reason the extreme values of ABCOP appear to come from near-exponential increases at higher areal densities (Figs. 6 and 10). Moreover, ABCOP may produce unexpected behavior, particularly in a small domain, because it is designed to capture the sparse local organizations of large domains, rather than assessing the domain as a whole. Nevertheless, ABCOP works effectively for most cases by following the principle that *the more individual convective cells occur, the higher the chance the scene is viewed as organized.*

Acknowledgments

We acknowledge funding from NASA's Precipitation Measurement Missions program. Resources supporting this work were provided by the NASA High-End Computing (HEC) Program through the NASA Center for Climate Simulation (NCCS) at Goddard Space Flight Center. We also thank three Reviewers who have helped to clarify and refine the study.

Open Research

The cloud-precipitation (hybrid) regime data and selected python codes to calculate ABCOP and other organization metrics are available at https://data.nasa.gov/Earth-Science/Tropical-CPR-identification-data-for-Organization-/md8t-ur38. IMERG precipitation data (V06 Final Run; doi: 10.5067/GPM/IMERG/3B-HH/06), Aqua/AIRS L3 Daily Standard Physical Retrieval (AIRS-only) 1 degree x 1 degree V7.0 (doi: 10.5067/UO3Q64CTTS1U) and NCEP/CPC Merged IR data (doi: 10.5067/P4HZB9N27EKU) were obtained from Goddard Earth Sciences Data and Information Services Center (GES DISC; https://disc.gsfc.nasa.gov/), Greenbelt, MD, USA. The Level-3 (L3) MODIS Atmosphere Daily Global Product (MYD08_D3, doi: 10.5067/MODIS/MYD08_D3.006) was obtained from the Level-1 and Atmosphere Archive & Distribution System (LAADS) Distributed Active Archive Center (DAAC; https://ladsweb.modaps.eosdis.nasa.gov/) in the Goddard Space Flight Center, Greenbelt, MD, USA. The OLR-based MJO index (OMI) data is available at https://psl.noaa.gov/mjo/mjoindex/omi.1x.txt. Niño3.4 SST index is provided by the NOAA/OAR/ESRL PSL, Boulder, Colorado, USA, from their Web site at https://psl.noaa.gov/gcos_wgsp/Timeseries/Nino34/.

Appendix

A1. Area-based interaction potential for the case of single aggregate

The new interaction potential based on area was defined in Eq. 6. For the case of single aggregate, we examine Eq. 6 with the condition of $A_j \rightarrow 0$ (thus also $r_j \rightarrow 0$). For convenience, L_{domain} is replaced by $\sqrt{A_{domain}}$, and Eqs. 5 and 6 are re-written as:

$$d_2(i,j) = max[d(i,j) - r_i, 1] \tag{A1}$$

$$V_{area}(i,j) = \frac{\left(\frac{A_i}{2}\right)/A_{domain}}{d_2(i,j)/\sqrt{A_{domain}}} = \frac{A_i}{2\sqrt{A_{domain}}}\frac{1}{d_2(i,j)} \tag{A2}$$

Here, the maximum value of *d(i,j)* varies depending on the shape of domain, and is *loosely approximated* as nominal diameter of domain, $2\sqrt{A_{domain}/\pi}$. Then, the range of $d_2(i,j)$ is estimated as:

$$1 \le d_2(i,j) \le 2\sqrt{A_{domain}/\pi} - \sqrt{A_i/\pi} \tag{A3}$$

where the nominal radius, r_i is replaced by $\sqrt{A_i/\pi}$. Then, the range of Eq. A2 is estimated using Eq. A3 as:

$$\frac{A_i}{2\sqrt{A_{domain}}}\frac{\sqrt{\pi}}{2\sqrt{A_{domain}}-\sqrt{A_i}} \le V_{area}(i,j) \le \frac{A_i}{2\sqrt{A_{domain}}} \tag{A4}$$

The left term of Eq. A4 can be simplified by introducing a new variable, $Density\_A_i = A_i/A_{domain}$:

$$\frac{\sqrt{\pi}}{2}\frac{Density\_A_i}{2-\sqrt{Density\_A_i}} \le V_{area}(i,j) \le \frac{A_i}{2\sqrt{A_{domain}}} \tag{A5}$$

From the range of V_{area} given in Eq. A5, and considering the proposition that a single aggregate has minimal “interaction potential,” we define the value of $V_{area}(i)$ as the smallest value in A5:

$$V_{area}(i) = \frac{\sqrt{\pi}}{2}\frac{Density\_A_i}{2-\sqrt{Density\_A_i}} \; for\ N = 1, with\ Density\_A_i = A_i/A_{domain} \tag{A6}$$

References

Bony, S., Semie, A., Kramer, R. J., Soden, B., Tompkins, A. M., & Emanuel, K. A. (2020). Observed Modulation of the Tropical Radiation Budget by Deep Convective Organization and Lower-Tropospheric Stability. *AGU Advances*, *1*(3), e2019AV000155. https://doi.org/10.1029/2019AV000155

Brune, S., Kapp, F., & Friederichs, P. (2018). A wavelet-based analysis of convective organization in ICON large-eddy simulations. *Quarterly Journal of the Royal Meteorological Society*, *144*(717), 2812–2829. https://doi.org/10.1002/qj.3409

Brune, S., Buschow, S., & Friederichs, P. (2020). Observations and high-resolution simulations of convective precipitation organization over the tropical Atlantic. *Quarterly Journal of the Royal Meteorological Society*, *146*(729), 1545–1563. https://doi.org/10.1002/qj.3751

Chen, S. S., Houze, R. A., & Mapes, B. E. (1996). Multiscale Variability of Deep Convection In Realation to Large-Scale Circulation in TOGA COARE. *Journal of the Atmospheric Sciences*, *53*(10), 1380–1409. https://doi.org/10.1175/1520-0469(1996)053<1380:MVODCI>2.0.CO;2

Chiu, S. N., Stoyan, D., Kendall, W. S., & Mecke, J. (Eds.). (2013). *Stochastic Geometry and its Applications* (1st ed.). Wiley. https://doi.org/10.1002/9781118658222

Coppin, D., & Bony, S. (2018). On the Interplay Between Convective Aggregation, Surface Temperature Gradients, and Climate Sensitivity. *Journal of Advances in Modeling Earth Systems*, *10*(12), 3123–3138. https://doi.org/10.1029/2018MS001406

Cronin, T. W., & Wing, A. A. (2017). Clouds, Circulation, and Climate Sensitivity in a Radiative-Convective Equilibrium Channel Model. *Journal of Advances in Modeling Earth Systems*, *9*(8), 2883–2905. https://doi.org/10.1002/2017MS001111

Hohenegger, C., & Stevens, B. (2016). Coupled radiative convective equilibrium simulations with explicit and parameterized convection. *Journal of Advances in Modeling Earth Systems*, *8*(3), 1468–1482. https://doi.org/10.1002/2016MS000666

Holloway, C. E., Wing, A. A., Bony, S., Muller, C., Masunaga, H., L’Ecuyer, T. S., et al. (2017). Observing Convective Aggregation. *Surveys in Geophysics*, *38*(6), 1199–1236. https://doi.org/10.1007/s10712-017-9419-1

Houze, R. A. (2004). Mesoscale convective systems. *Reviews of Geophysics*, *42*(4), RG4003. https://doi.org/10.1029/2004RG000150

Huffman, G. J., Stocker, E. F., Bolvin, D. T., Nelkin, E. J., & Tan, J. (2019). GPM IMERG Final Precipitation L3 Half Hourly 0.1 degree x 0.1 degree V06, Greenbelt, MD, Goddard Earth Sciences Data and Information Services Center (GES DISC) [Data set]. Greenbelt, MD: NASA Goddard Earth Sciences Data and Information Services Center. https://doi.org/10.5067/GPM/IMERG/3B-HH/06

Huffman, G. J., Bolvin, D. T., Braithwaite, D., Hsu, K., Joyce, R., Kidd, C., et al. (2019, March 13). Algorithm Theoretical Basis Document (ATBD) version 06. NASA Global Precipitation Measurement (GPM) Integrated Multi-satellitE Retrievals for GPM (IMERG). https://gpm.nasa.gov/sites/default/files/document_files/IMERG_ATBD_V06_0.pdf. NASA. Retrieved from https://gpm.nasa.gov/sites/default/files/document_files/IMERG_ATBD_V06_0.pdf

Janowiak, J., Joyce, B., & Xie, P. (2017). NCEP/CPC L3 Half Hourly 4km Global (60S - 60N) Merged IR V1 [Data set]. NASA Goddard Earth Sciences Data and Information Services Center. https://doi.org/10.5067/P4HZB9N27EKU

Jin, D., Oreopoulos, L., Lee, D., Tan, J., & Kim, K. (2020). Large-Scale Characteristics of Tropical Convective Systems Through the Prism of Cloud Regime. *Journal of Geophysical Research: Atmospheres*, *125*(6), e2019JD021157. https://doi.org/10.1029/2019JD031157

Jin, D., Oreopoulos, L., Lee, D., Tan, J., & Cho, N. (2021). Cloud–Precipitation Hybrid Regimes and Their Projection onto IMERG Precipitation Data. *Journal of Applied Meteorology and Climatology*, *60*(6), 733–748. https://doi.org/10.1175/JAMC-D-20-0253.1

Kadoya, T., & Masunaga, H. (2018). New Observational Metrics of Convective Self-Aggregation: Methodology and a Case Study. *Journal of the Meteorological Society of Japan. Ser. II*, *96*(6), 535–548. https://doi.org/10.2151/jmsj.2018-054

Kahn, B. H., Irion, F. W., Dang, V. T., Manning, E. M., Nasiri, S. L., Naud, C. M., et al. (2014). The Atmospheric Infrared Sounder version 6 cloud products. *Atmospheric Chemistry and Physics*, *14*(1), 399–426. https://doi.org/10.5194/acp-14-399-2014

Kiladis, G. N., Dias, J., Straub, K. H., Wheeler, M. C., Tulich, S. N., Kikuchi, K., et al. (2014). A Comparison of OLR and Circulation-Based Indices for Tracking the MJO. *Monthly Weather Review*, *142*(5), 1697–1715. https://doi.org/10.1175/MWR-D-13-00301.1

Laing, A. G., & Fritsch, J. M. (1997). The global population of mesoscale convective complexes. *Quarterly Journal of the Royal Meteorological Society*, *123*(538), 389–405. https://doi.org/10.1002/qj.49712353807

Madden, R. A., & Julian, P. R. (1971). Detection of a 40–50 Day Oscillation in the Zonal Wind in the Tropical Pacific. *Journal of Atmospheric Sciences*, *28*(5), 702–708. https://doi.org/10.1175/1520-0469(1971)028<0702:DOADOI>2.0.CO;2

Madden, R. A., & Julian, P. R. (1994). Observations of the 40–50-Day Tropical Oscillation—A Review. *Monthly Weather Review*, *122*(5), 814–837. https://doi.org/10.1175/1520-0493(1994)122<0814:OOTDTO>2.0.CO;2

Mapes, B. E., & Houze, R. A. (1993). Cloud Clusters and Superclusters over the Oceanic Warm Pool. *Monthly Weather Review*, *121*(5), 1398–1416. https://doi.org/10.1175/1520-0493(1993)121<1398:CCASOT>2.0.CO;2

Nakazawa, T. (1988). Tropical Super Clusters within Intraseasonal Variations over the Western Pacific. *Journal of the Meteorological Society of Japan.*, *66*(6), 823–839. https://doi.org/10.2151/jmsj1965.66.6_823

Nesbitt, S. W., Zipser, E. J., & Cecil, D. J. (2000). A Census of Precipitation Features in the Tropics Using TRMM: Radar, Ice Scattering, and Lightning Observations. *Journal of Climate*, *13*(23), 4087–4106. https://doi.org/10.1175/1520-0442(2000)013<4087:ACOPFI>2.0.CO;2

Oreopoulos, L., Cho, N., Lee, D., Kato, S., & Huffman, G. J. (2014). An examination of the nature of global MODIS cloud regimes. *Journal of Geophysical Research: Atmospheres*, *119*(13), 8362–8383. https://doi.org/10.1002/2013JD021409

Oreopoulos, L., Cho, N., Lee, D., & Kato, S. (2016). Radiative effects of global MODIS cloud regimes. *Journal of Geophysical Research: Atmospheres*, *121*(5), 2299–2317. https://doi.org/10.1002/2015JD024502

Platnick, S., King, M. D., Ackerman, S. A., Menzel, W. P., Baum, B. A., Riedi, J. C., & Frey, R. A. (2003). The MODIS cloud products: algorithms and examples from terra. *IEEE Transactions on Geoscience and Remote Sensing*, *41*(2), 459–473. https://doi.org/10.1109/TGRS.2002.808301

Platnick, S., Meyer, K. G., King, M. D., Wind, G., Amarasinghe, N., Marchant, B., et al. (2018, July). MODIS cloud optical properties: User guide for the collection 6/6.1 Level-2 MOD06/MYD06 product and associated Level-3 datasets, Version 1.1. https://atmosphere-imager.gsfc.nasa.gov/sites/default/files/ModAtmo/MODISCloudOpticalPropertyUserGuideFinal_v1.1_1.pdf. Retrieved from https://atmosphere-imager.gsfc.nasa.gov/sites/default/files/ModAtmo/MODISCloudOpticalPropertyUserGuideFinal_v1.1_1.pdf

Retsch, M. H., Jakob, C., & Singh, M. S. (2020). Assessing Convective Organization in Tropical Radar Observations. *Journal of Geophysical Research: Atmospheres*, *125*(7), e2019JD031801. https://doi.org/10.1029/2019JD031801

Susskind, J., Blaisdell, J. M., & Iredell, L. (2014). Improved methodology for surface and atmospheric soundings, error estimates, and quality control procedures: the atmospheric infrared sounder science team version-6 retrieval algorithm. *Journal of Applied Remote Sensing*, *8*(1), 084994. https://doi.org/10.1117/1.JRS.8.084994

Tan, J., Huffman, G. J., Bolvin, D. T., & Nelkin, E. J. (2019). IMERG V06: Changes to the Morphing Algorithm. *Journal of Atmospheric and Oceanic Technology*, *36*(12), 2471–2482. https://doi.org/10.1175/JTECH-D-19-0114.1

Tobin, I., Bony, S., & Roca, R. (2012). Observational Evidence for Relationships between the Degree of Aggregation of Deep Convection, Water Vapor, Surface Fluxes, and Radiation. *Journal of Climate*, *25*(20), 6885–6904. https://doi.org/10.1175/JCLI-D-11-00258.1

Tompkins, A. M., & Semie, A. G. (2017). Organization of tropical convection in low vertical wind shears: Role of updraft entrainment. *Journal of Advances in Modeling Earth Systems*, *9*(2), 1046–1068. https://doi.org/10.1002/2016MS000802

Weger, R. C., Lee, J., Zhu, T., & Welch, R. M. (1992). Clustering, randomness and regularity in cloud fields: 1. Theoretical considerations. *Journal of Geophysical Research: Atmospheres*, *97*(D18), 20519–20536. https://doi.org/10.1029/92JD02038

White, B. A., Buchanan, A. M., Birch, C. E., Stier, P., & Pearson, K. J. (2018). Quantifying the Effects of Horizontal Grid Length and Parameterized Convection on the Degree of Convective Organization Using a Metric of the Potential for Convective Interaction. *Journal of the Atmospheric Sciences*, *75*(2), 425–450. https://doi.org/10.1175/JAS-D-16-0307.1

Windmiller, J. M., & Craig, G. C. (2019). Universality in the Spatial Evolution of Self-Aggregation of Tropical Convection. *Journal of the Atmospheric Sciences*, *76*(6), 1677–1696. https://doi.org/10.1175/JAS-D-18-0129.1

Wing, A. A. (2019). Self-Aggregation of Deep Convection and its Implications for Climate. *Current Climate Change Reports*, *5*(1), 1–11. https://doi.org/10.1007/s40641-019-00120-3

Wing, A. A., Emanuel, K., Holloway, C. E., & Muller, C. (2017). Convective Self-Aggregation in Numerical Simulations: A Review. *Surveys in Geophysics*, *38*(6), 1173–1197. https://doi.org/10.1007/s10712-017-9408-4

Wing, A. A., Stauffer, C. L., Becker, T., Reed, K. A., Ahn, M., Arnold, N. P., et al. (2020). Clouds and Convective Self-Aggregation in a Multimodel Ensemble of Radiative-Convective Equilibrium Simulations. *Journal of Advances in Modeling Earth Systems*, *12*(9), 1–38. https://doi.org/10.1029/2020MS002138

Worku, L. Y., Mekonnen, A., & Schreck, C. J. (2019). Diurnal cycle of rainfall and convection over the Maritime Continent using TRMM and ISCCP. *International Journal of Climatology*, *39*(13), 5191–5200. https://doi.org/10.1002/joc.6121

Xu, K., Hu, Y., & Wong, T. (2019). Convective Aggregation and Indices Examined from CERES Cloud Object Data. *Journal of Geophysical Research: Atmospheres*, *124*(24), 13604–13624. https://doi.org/10.1029/2019JD030816

Yang, G., Hoskins, B., & Slingo J. (2003). Convectively Coupled Equatorial Waves: A New Methodology For Identifying Wave Structures In Observational Data. *Journal of the Atmospheric Science*, 60(14), 1637–1654. https://doi.org/10.1175/1520-0469(2003)060<1637:CCEWAN>2.0.CO;2

Yuan, J., & Houze, R. A. (2010). Global Variability of Mesoscale Convective System Anvil Structure from A-Train Satellite Data. *Journal of Climate*, *23*(21), 5864–5888. https://doi.org/10.1175/2010JCLI3671.1